

# Experimental Investigation of Interfacial Conditions between Fluid and Porous Layer Formed by Periodic Arrays of Circular and Non-Circular Cylinders

A. CIHAT BAYTAŞ<sup>a</sup>, D. ERDEM<sup>a,\*</sup>, H. ACAR<sup>a</sup>, O. CETINER<sup>a</sup> AND H. BAŞCI<sup>b</sup>

<sup>a</sup>Faculty of Aeronautics and Astronautics, Istanbul Technical University, Istanbul, Turkey

<sup>b</sup>Aerodynamics Division, TUBITAK, SAGE, Ankara, Turkey

(Received January 8, 2018)

In this experimental study, a flow through a two-dimensional channel partially containing porous media is investigated. A two-layer structure comprising of a saturated porous layer with an overlaying fluid flow layer in a rectangular horizontal channel is designed for the experiments. Flow characteristics at the interface between clear fluid and porous layer are investigated. The porous layer consists of cylindrical rod bundle placed horizontally on the side walls of the channel in arranged square arrays. In the experiments, water white oil is used as the working fluid to match the refractive index of the cylindrical rods made of Plexiglas. Visualizations and measurements have been acquired by digital particle image velocimetry system for the velocity profiles which help us to evaluate the interface velocity and slip coefficient at the interface region. The measurement of interface velocity profile is repeated for circular, square, and 45° rotated square cylindrical rods to understand the effects of the structure of the interface region. It has been observed that dimensionless slip or interface velocity depends significantly on the surface structure at the interface region when cylindrical rods each with circular, square, and 45° rotated square cross-sections are used as porous medium. The volumetric flow rate can be changed according to the cross-sections of cylindrical rods. The permeability for the different arrangements of cylindrical rods is computed by an analytical study. The dimensionless slip velocity, slip coefficient, particle image velocimetry images, experimental and numerical velocity vector maps, and velocity profiles at the interface are presented.

DOI: [10.12693/APhysPolA.133.1314](https://doi.org/10.12693/APhysPolA.133.1314)

PACS/topics: flows through porous media, interfacial flows, interface slip coefficient, interface geometry, composite channel, PIV, boundary condition

## 1. Introduction

Transport phenomena occurring at the region between porous and clear fluid layers are frequently encountered in many technological and scientific applications. Some of the important applications are benthic boundary layers, drying processes, geophysical fluid dynamics, environmental hydraulics, thermal insulation, storage of nuclear waste, ground water pollution, heat pipes, and boundary layer suction for aircraft wings, etc. The subject of this study is of interest in a number of fields related with environmental flows and industrial flows in general. In this study, fluid layer and porous layer are named as clear fluid and porous regions, respectively. In addition, the boundary between clear fluid and porous layers is named as interface region. Transport phenomena at the interface region and its boundary conditions are not very well known for different parameters such as porosity, permeability, flow velocity and interface region structure. The slip condition is valid at the interface region and an effective slip velocity is essentially required at the interface. For this reason, the effective slip velocity has to be improved or refined by new experimental and theoretical investigations to clarify and see how the slip

velocity at the interface is affected by both the porous medium and the clear fluid region.

A pioneering experimental study about boundary conditions was accomplished at the interface by Beavers and Joseph [1]. They performed experiments for a viscous fluid using a two-dimensional channel with a non-permeable upper and a permeable lower wall (interface region) to investigate laminar flow. In their experiments, the pressure gradient on the flow direction was ensured to be uniform in the composite channel. They established the boundary condition at the interface in terms of a dimensionless slip coefficient  $\alpha$ , the values of which were found to be of order unity. Gupte and Advani [2] performed an experimental study by using laser Doppler anemometry to investigate the flow near the interface region for a composite channel which included a clear fluid and a porous layer. They measured the local velocity profile inside the porous channel. They investigated the effect of fluid flow rate, fluid viscosity, permeability of the porous layer and the gap width between the parallel plates on the interface velocity profile, and the velocity profile for channel cross-section. They found out that the boundary layer area was proportional to the channel depth and it was greater than the square root of the permeability. Alazmi and Vafai [3] gave an overview of the interfacial conditions for heat transfer and fluid flow. They proposed an inclusive analysis of differing what within the diffusion phenomena at the interface region. Goharzadeh et al. [4] employed the refractive index

\*corresponding author; e-mail: [erdem@itu.edu.tr](mailto:erdem@itu.edu.tr)

matching (RIM) and particle image velocimetry (PIV) techniques to measure the flow field at the fluid-porous interface. They used transparent glass beads of different diameters to form the porous media. They measured the velocity profile and interface velocity for different permeability and porosity. They also found out that the vertical velocity gradient depends vigorously on the height of the fluid layer in their experimental study.

Many scientists have used the PIV measurement technique to determine the interface velocity and the velocity profile in the composite porous channel. Some of the researchers used spherical glass beads to form their porous layer and some of them used cylindrical rods that have different cross-sections (circular, square, triangular, etc.). Shams et al. [5] used PIV technique in their experiment containing an annular array of equally spaced circular cylinders to investigate the flow field near the layer of porous medium. Tachie et al. [6] performed an experiment using PIV to measure the velocity in square arrays of rods where the cross-sections were circular, triangular, and square. They investigated the circulation formation and its relationship with rod geometry and solid volume fraction. The rods were placed perpendicular to the direction of the flow and the range of the solid volume fraction of the array was between 0.01 and 0.16. By using PIV, Tachie et al. [7] measured velocity in a circular Couette flow in a brush. They used rod arrays installed in a fixed inner cylinder with several solid volume fractions such as 0.025, 0.05, and 0.1.

Agelinchaab et al. [8] performed experiments to determine the slip velocity at the interface of fluid and porous layer in a two-dimensional rectangular channel. Their channel had vertical acrylic circular cylinders mounted at the bottom. The circular cylinders were placed with equal spacing as square arrays. They investigated the effects of the height of the vertical cylinders, the porosity, and the permeability of the cylinders on the interface velocity. They found out that the values of the interface velocity (slip) depends on the height of the cylinders and permeability. Furthermore, their work dealt with the amounts of penetration of the flow in the porous medium. Narasimhan et al. [9] performed an experimental and numerical simulation using layered type parallel plates as a porous medium. Their aim was to obtain the interface slip coefficient by using PIV. They especially investigated the effects of the permeability on the slip coefficient. James and Davis [10] emphasized that the slip coefficient is a function of geometry only. As a result, the slip coefficient is considered to be dependent on the porous medium pattern and not on the fluid viscosity. Most of the available studies on transport phenomena at the interface region in a channel consider a partially filled porous layer and a clear fluid layer. The main goal of the present study is to investigate the slip coefficient and the interface velocity for different geometrical structures at the interface region. However, the slip coefficient and interface velocity are strongly affected by the surface geometry or structure at the interface region.

The main focus and the contribution of the present study are to consider the effect of the shape of cylindrical rod's cross-section at the interface region on interface velocity and slip coefficient. In the experiments, the cross-sections of the rods are circular, square and 45° rotated square. The channel flow rate, the height of fluid and porous layers are kept constant.

A similar study, which uses different cross-sections of rods especially the square rod and 45° rotated square rod to determine the effect of interface geometry on interface velocity, has not been encountered in the literature yet. The investigation is complemented by computational fluid dynamics (CFD) to support the experimental results on flow behaviour and structures. The PIV images, experimental and numerical velocity vector maps, streamlines at interface region, and velocity profile at the interface region are presented.

## 2. Mathematical background and problem formulation

The fluid flow in porous media was analysed by using Darcy's empirical law, Nield and Bejan [11]. The Darcy famous law is expressed as

$$\langle u \rangle = -\frac{k}{\mu} \nabla \langle p \rangle \quad (1)$$

where  $\langle u \rangle$  [m/s] is a superficial velocity of a porous medium,  $k$  [m<sup>2</sup>] is the permeability of porous media,  $\nabla \langle p \rangle$  [N/m<sup>3</sup>] is local pressure gradient and  $\mu$  is dynamic viscosity of fluid. When the flow of clear fluid region seen in Fig. 1 exhibits the Poiseuille motion behaviour, it may

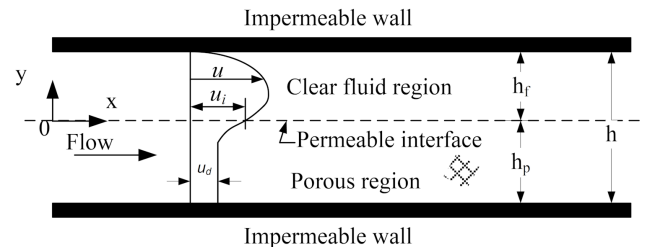


Fig. 1. Schematic diagram of a 2D rectilinear flow for experimental composite channel.

be defined by the Stokes equation. The steady Stokes equation in  $x$  direction is written by

$$\frac{d^2 u}{dy^2} = \frac{1}{\mu} \frac{dp}{dx} \quad (2)$$

The Darcy equation in Eq. (1) is defined as a first order partial differential equation, whereas Stokes equation given in Eq. (2) represents a second-order partial differential equation. The Brinkman equation given in Eq. (3), which has the same order as the Stokes equation, should be used for the Darcy flow to be able to develop a mathematical model matching the Stokes flow with the Darcy flow. Note that the Brinkman equation guarantees shear stresses at the interface and continuity in velocity

$$\frac{\mu \langle u \rangle}{k} = -\frac{dp}{dx} + \mu_{eff} \frac{d^2 \langle u \rangle}{dy^2}, \quad (3)$$

where  $\mu_{eff}$  denotes effective viscosity of the fluid in the porous medium. The effective viscosity can be related to the fluid and the porous medium structure. The slip flow boundary condition at the interface was given by Beavers and Joseph [1] as follows:

$$\left. \frac{du}{dy} \right|_{y=0} = \frac{\alpha}{\sqrt{k}} (u_i - u_d), \quad (4)$$

where  $u_i$  is the interface velocity,  $u_d$  is the Darcy velocity and  $\alpha$  is an interface slip coefficient. The slip coefficient,  $\alpha$ , which is a dimensionless quantity, depends on the structure of the porous material at the interface area. Furthermore,  $\alpha$  also relies on the local geometry of the interface except the fluid characteristics. By using the empirical boundary conditions at the interface proposed by Beavers and Joseph [1], the analytical solution of Eq. (3) can be formulated as follows, according to Gupte and Advani [2]:

$$\langle u \rangle = u_d + (u_i - u_d) \exp\left(-\frac{y}{(\mu_{eff}/\mu)^{1/2} \sqrt{k}}\right). \quad (5)$$

Accompanied by the boundary conditions, see Fig. 1:

$$\begin{aligned} \langle u \rangle &= u_i \quad \text{at} \quad y = 0, \\ \langle u \rangle &= u_d \quad \text{at} \quad y \rightarrow -\infty \end{aligned} \quad (6)$$

If Eq. (5) is derived with respect to  $y$  for  $y = 0$ , the shear rate at the interface is obtained as follows, by Gupte and Advani [2] and Agelinchaab et al. [8]:

$$\left. \frac{du}{dy} \right|_{y=0} = \frac{1}{(\mu_{eff}/\mu)^{1/2} \sqrt{k}} (u_i - u_d). \quad (7)$$

The slip coefficient  $\alpha$  from Eq. (4) is equivalent to  $(\mu_{eff}/\mu)^{-1/2}$  as seen in Eq. (7). Interface velocity as a boundary condition can be specified by using the Brinkman Eq. (3) and Beavers–Joseph formulation (4) as shown in Eq. (7). The interface (or slip) velocity depends on solid fraction of the porous medium. The interface velocity  $u_i$  is related to the external shear rate at the interface and it was defined by James and Davis [10] in terms of the dimensionless interface (or slip) velocity,  $u_i/\gamma\sqrt{k}$ .

Here  $\sqrt{k}$  is the length scale for the porous medium,  $u_i/\gamma$  is a measure of the depth of penetration and  $\gamma = du/dy$  is the shear rate at the interface. Non-dimensional interface velocity is independent of solid volume fraction or rod spacing. However, it depends only on the ratio of the height of porous region to that of channel and is kept as a constant in the present study. The slip coefficient  $\alpha$  can be determined from experimental measurements of  $u_i$ ,  $u_D$  and  $du/dy$  at the interface. In the experimental study,  $u_i$  and  $du/dy$  are evaluated at  $y = 0$  and  $u_d$  is evaluated at distance from the interface plane. All experimentally measured values can be seen in Table I.

TABLE I

Outline of significant experimental flow parameters.

	$\beta$	$u_b$ [ $\times 10^3$ m/s]	$u_{max}$ [ $\times 10^3$ m/s]	$u_i$ [ $\times 10^3$ m/s]	$u_d$ [ $\times 10^3$ m/s]	$k$ [m <sup>2</sup> ]	$Re_p$	$\gamma$	$\alpha$	$u_i/\gamma\sqrt{k}$
case-1 circular	0.178	7.540	10.846	2.869	0.651	$1.37 \times 10^{-5}$	0.32	0.9951	1.661	0.779
case-2 square	0.227	7.709	11.356	1.768	0.503	$9.75 \times 10^{-6}$	0.25	1.0822	2.671	0.523
case-3 45° rotated square	0.113	7.098	10.224	2.855	0.705	$2.1 \times 10^{-5}$	0.35	0.8954	1.909	0.696

### 2.1. Permeability for different cross-sections of rods

There are three cases in this experimental study as seen in Fig. 2: the cross-sections of the rods are circular for case-1, square for case-2 and 45° rotated square for case-3. The analytical expressions of the permeability are available in the open literature. Jackson and James [12] and Tamayol and Bahrami [13] calculated permeability analytically for case-1. Moreover, Baytas et al. [14] suggested a new idea to derive the analytical expressions of the permeability for case-1, case-2, and case-3. Calculation of permeability for case-1 is given by Baytas et al. [14] as

$$k = D^2 \left\{ \frac{12 (\sqrt{\beta'} - 1)}{\beta' \sqrt{\beta'}} \left[ \frac{6 - g(\varepsilon)}{6} \right] + \frac{12 (\beta' + 1/2)}{\sqrt{\beta'} (\beta' - 1)^2} + \frac{18\sqrt{\beta'} \left[ \tan^{-1} \left( (\beta' - 1)^{-1/2} \right) + \frac{\pi}{2} \right]}{(\beta' - 1)^{5/2}} \right\}^{-1}, \quad (8)$$

where  $\beta' = \pi/4\beta$ ,  $g(\varepsilon) = 1.274\varepsilon - 0.274$  and  $\beta = 1 - \varepsilon$ . The porosity for circular cylinder is  $\varepsilon = 1 - \frac{\pi}{4} \left(\frac{D}{S}\right)^2$ .

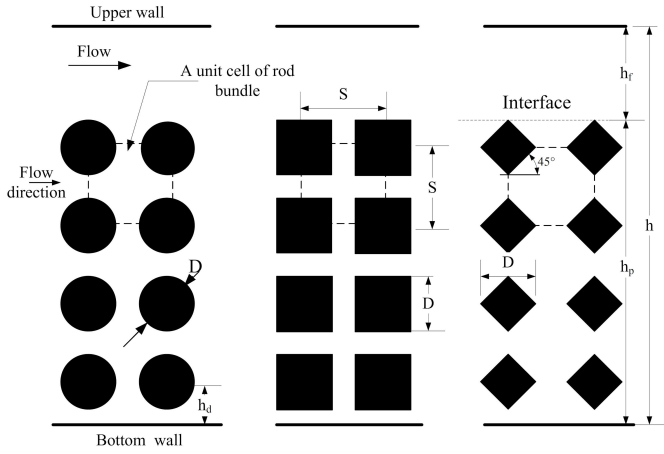


Fig. 2. Rectangular arrangements of parallel cylindrical rods toward normal flow (see Table II).

TABLE II

Parameters of circular, square and rotated square cylinders.

Case 1 Circular cylinder	Case 2 Square cylinder	Case 3 Rotated square cylinder
$S = 21 \text{ mm}$	$S = 21 \text{ mm}$	$S = 21 \text{ mm}$
$D = 10 \text{ mm}$	$D = 10 \text{ mm}$	$D = 10 \text{ mm}$
$h_f = 34 \text{ mm}$	$h_f = 34 \text{ mm}$	$h_f = 34 \text{ mm}$
$h_p = 74 \text{ mm}$	$h_p = 74 \text{ mm}$	$h_p = 74 \text{ mm}$
$h_d = 6 \text{ mm}$	$h_d = 6 \text{ mm}$	$h_d = 6 \text{ mm}$
$\varepsilon = 0.822$	$\varepsilon = 0.773$	$\varepsilon = 0.887$
$\beta = 1 - \varepsilon = 0.178$	$\beta = 1 - \varepsilon = 0.227$	$\beta = 1 - \varepsilon = 0.113$
$k = 1.37 \times 10^{-5}$	$k = 0.975 \times 10^{-5}$	$k = 2.1 \times 10^{-5}$
(Eq.(8))	(Eq.(9))	(Eq.(10))
Row = 4	Row = 4	Row = 4

Calculation of permeability for case-2 is as follows, Baytas et al. [14]:

$$k = D^2 \left\{ 12 \left( \frac{1}{\sqrt{\beta}} - 1 \right)^{-3} + 12\beta \left( 1 - \sqrt{\beta} \right) \left[ \frac{6 - g(\varepsilon)}{6} \right] \right\}^{-1} \quad (9)$$

where  $g(\varepsilon) = \varepsilon$  and  $\beta = 1 - \varepsilon$ . The porosity for square cylinder is  $\varepsilon = 1 - \left(\frac{D}{S}\right)^2$ .

Calculation of permeability for case-3 is as follows, Baytas et al. [14]:

$$k = D^2 \left\{ 6 \left( \frac{1}{\sqrt{2\beta}} - 1 \right)^{-2} - 12\beta + 24\beta \left( 1 - \sqrt{2\beta} \right) \left[ \frac{6 - g(\varepsilon)}{6} \right] \right\}^{-1}, \quad (10)$$

where  $g(\varepsilon) = 2\varepsilon = 1$  and  $\beta = 1 - \varepsilon$ . The porosity for 45° rotated square cylinder is  $\varepsilon = 1 - \frac{1}{2} \left(\frac{D}{S}\right)^2$ .

### 3. Experimental setup and measurement techniques

In this experimental study, the composite system consists of a clear fluid layer and a horizontal porous layer as shown schematically in Fig. 1. The experiments are carried out in a rectangular channel whose test section is made of transparent Plexiglas (acrylic) and its dimensions are  $200 \text{ mm} \times 129 \text{ mm} \times 2000 \text{ mm}$ . The porous layer is 1000 mm long with an effective flow area of 109 mm by 180 mm as illustrated schematically in Fig. 3. A bundle of solid rods is placed perpendicular to the flow with a non-staggered arrangement to simulate the porous layer. The properties and dimensions of all three cases used in the experiments are given in Fig. 2. The geometrical values and structure of the rod bundles are inspired by the studies of Prinos et al. [15] and Chan et al. [16]. The length of the rods is 180 mm. They are also made of transparent Plexiglas whose refractive index is 1.49. The rods are equally spaced in the square arrays and extended to the full channel width. As seen in Fig. 3,  $x$ -axis denotes the stream wise direction and  $y$  — the vertical direction. In the experiments, the NT22 WOFLEX water white oil was used as a working fluid. Refractive index of the water white oil is 1.49, the same as Plexiglas rods and the kinematic viscosity of working fluid is determined to be  $20 \text{ mm}^2/\text{s}$  at  $23^\circ\text{C}$  by using a rheometer with a  $\pm 1.0\%$  accuracy. The optical distortion of the laser sheet passing through the refractive media is minimized by selecting this oil whose refractive index is same as the rod.

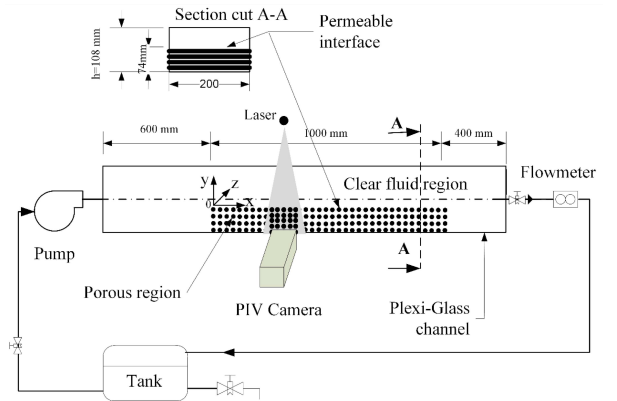


Fig. 3. Schematic diagram of experimental setup.

The experimental setup consists of a tank, pump, driver, and a flow meter. The motor speed of the pump is controlled by an analogue potentiometer with linear  $V/f$ . The pump has a flow rate range of  $0.0 - 2.4 \text{ m}^3/\text{h}$ . The flow rate is measured by an electromagnetic flow meter. During the experiments, the magnitude of the flow rate was set to  $0.16 \text{ m}^3/\text{h}$  for three cross-section of the rods. The Reynolds number based on the clear fluid height of channel is  $\text{Re} \cong 11$ . The clear fluid height,  $h_f$ , is kept constant in this study. Our basic motivation is to investigate the effect of the shape of the cylindrical

rod's cross-section at the interface region on the interface velocity and the slip coefficient. Investigated Reynolds numbers based on the rod diameter and Darcy velocity,  $Re_p$ , are 0.32, 0.25, and 0.35 for case-1, case-2 and case-3, respectively as seen in Table I. To calculate the Reynolds number, the characteristic length is defined as the diameter for the circular rods, side length for square rods and diagonal length for  $45^\circ$  rotated square rods. The flow is visualized quantitatively using a DPIV system. The seeding particles are selected to be silver-coated hollow glass spheres (S-HGS) with an average diameter of  $10 \mu m$ . A flow Sense 2M camera with  $1600 H \times 1200 V$  pixel resolution was used to acquire the images of the flow field. The illumination is provided by an Nd/YAG laser which has two cavities each with a 15 Hz repetition rate and maximum energy of  $120 mJ/pulse$ . Laser, camera, and PC communicate physically and are synchronized by a timer box and controlled via Dantec Dynamic Studio software. For each experiment, two sets of at least 475 images were acquired at 10 Hz double frame rate. The camera was translated vertically to 8 positions in order to cover all the channel depth. Accurate positioning of the camera was achieved using a traversing mechanism. For the post-processing, image pairs are cross-correlated; correlation window size is  $64 \times 64$  pixels and correlation windows are overlapped 50% in each direction. At the final stage, velocity vector mesh is  $0.57 mm \times 0.57 mm$  in the plane of the flow. The total velocity uncertainty in the DPIV experiments is less than 2%. Velocity fields are time-averaged at the final processing stage. The resulting velocity data lets us to evaluate the Brinkman layer thickness.

#### 4. Computational procedure

A computational solution for the system is performed using CFD code Fluent to compare the experimental results with computational ones. A full scale 3D model of the channel same as the one used at the experimental process is designed for the computational work and the porous media consisting of the circular, square, and  $45^\circ$  rotated square cross-sectioned rods are added to this model to investigate all three cases. A grid independence check is carried out for all three cases and adequate grid sizes are determined to perform the computational work with enough accuracy. Grids of three different sizes, approximately 8 million, 12 million and 15 million cells, are generated. To check the contribution of using 12 million or 15 million cells instead of 8 million, the interface velocity and the maximum velocity are compared only for the case-1 for brevity in Table III. As seen in Table III, the percentage of difference between 8 and 12 million and 8 and 15 million cells is less than 2 percent. Therefore, a grid as 8 million cells is chosen for all calculations. It could not be feasible to generate a grid with lower number of cells due to the complexity of the geometry. The grid is generated using unstructured hexahedral/wedge elements for all cases and cell counts 8 million are reached regarding the case modelled. No slip boundary condition

(wall boundary condition) is employed for all of the solid boundaries of the system which are the walls surrounding the channel and the surfaces of the rods. Velocity inlet boundary condition is set for the entrance of the channel and the pressure outlet boundary condition for the out-flow region. In the solution process, coupled mass and momentum equations are dealt with steady and laminar flow conditions which are the same physical conditions of the experimental work. For discretization, second order upwind method is applied for momentum equations to have increased accuracy. Standard scheme is applied for pressure term discretization. SIMPLE algorithm of Patankar [17] is applied for pressure and velocity coupling. Solution is obtained using double precision solver and the iterations are run until the residuals drop six orders in magnitude ( $10^{-6}$ ). Furthermore, the conservation of mass is checked by means of inlet and outlet values of the mass flow rate to ensure the convergence (convergence criterion is  $10^{-6}$ ).

TABLE III

Accuracy test at steady state for 8 million cells in comparison with either 12 and or 15 million cells.

Cells	Percentage of difference [%]	
	Interface velocity	Maximum velocity
8 million in comparison with 12 million	1.5	0.6
8 million in comparison with 15 million	1.8	0.7

#### 5. Results and discussion

In this study, several velocity measurements are also carried out in the channel without rod bundle, at different locations from inlet to outlet of the channel. Obtained velocity profiles of laminar flow from the experiments for clear fluid in the channel are best matched with the analytical fully developed profile in the channel shown in Fig. 4. It is evidently observed from Fig. 4 that the ratio of maximum centerline velocity in the channel to the bulk velocity is 1.5 as well known. The comparison shows good match, where the maximum error is less than 5%, between the experimental and analytical results.

It is assumed that the channel width in the direction of perpendicular to the flow (in  $z$ -direction) is long enough to eliminate any end effects. This can be evidently explained by Fig. 5. The velocities are unchanged and symmetric about the middle of the channel in  $z$  direction for case-1 as seen in Fig. 5. The velocity profiles at  $z$  direction are computed for all three cases at different  $y$  locations in clear fluid and porous layer regions but not presented here for case-2 and case-3 for brevity.

The PIV images are illustrated in Fig. 6 for the three cases. The PIV images demonstrate the interface region



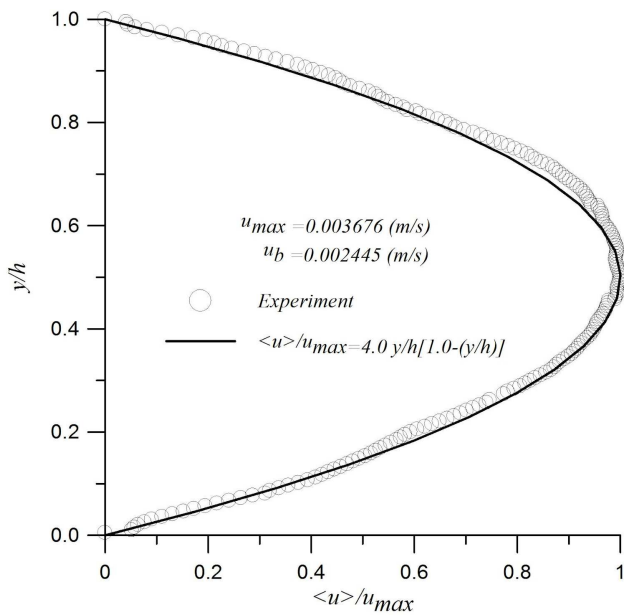


Fig. 4. Velocity profile for empty channel at  $x = 677$  mm.

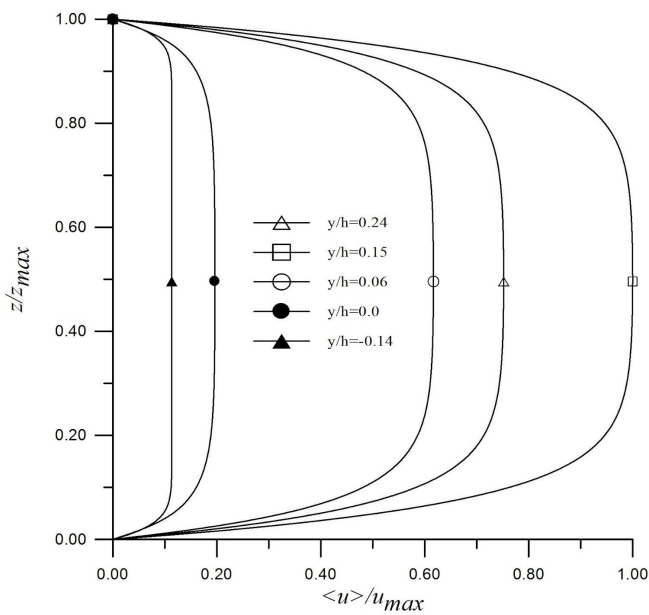


Fig. 5. Numerical velocity profiles  $u(z)$  at various  $y$  locations for case-1.

with a field of view of  $2.9 \times 2.9 \text{ cm}^2$ . Even though the main attention is focused on the interface region in this study, the flow characteristics in the whole channel is examined by vertically moving PIV camera from upper to lower wall regions with a computer controlled traversing mechanism. The upper section of Fig. 6 is the clear fluid region while the lower section is the porous layer region of the channel. The horizontal velocity component is zero at the rod surfaces. The horizontal velocity component de-

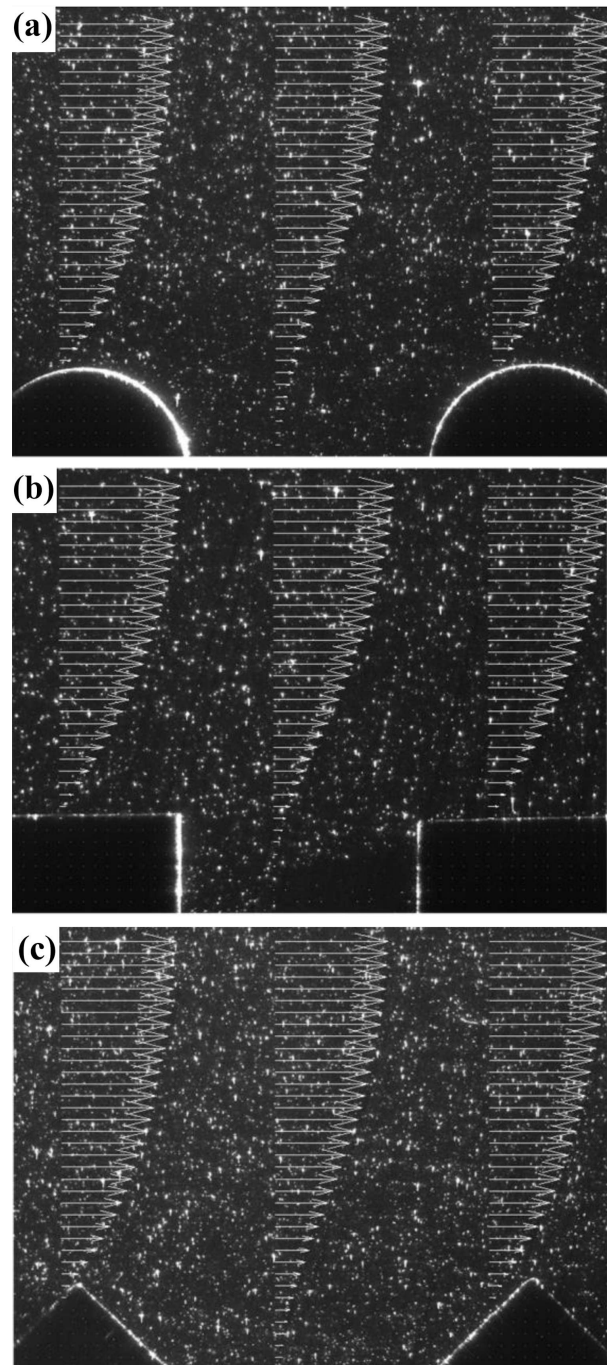


Fig. 6. PIV images on  $x-y$  plane with a field of view  $(2.9 \times 2.9 \text{ cm}^2)$  and their vertical averaged profile for horizontal velocity components: (a) case-1, (b) case-2, (c) case-3.

creases continuously until it reaches the interface region of the porous layer as seen in Fig. 6 for the three cases.

The streamlines near the interface and between rods for three cases are illustrated in Fig. 7 along with those obtained numerically. The velocities in the clear fluid layer are much greater than the velocities of the porous layer. The velocity vectors in the porous layer are very small and nearly invisible as their magnitudes are smaller

than those in the clear fluid. The fluid particles in the clear fluid region move on a straight line trajectory but in the interface region they change trajectory due to the geometry of interface region. The fluid particle trajectories strongly depend on the surface roughness or shape of the interface. This can be observed in Fig. 7b and c. In Fig. 7b, a recirculation is observed between square cylinders at the interface region while it disappears from second row to downward. This strong circulation causes

a blockage and fluid flow is stopped between square cylinders. As a result, the interface velocity is decreased as seen in Table I. The velocity vectors between square cylinders are visible and move on a straight line trajectory. The fluid flow is hindered between two square cylinders at the interface as seen evidently from streamlines. A strong cell occurs between two square cylinders due to this blockage at just the interface region but there are not any cells at the second row from interface to downward.

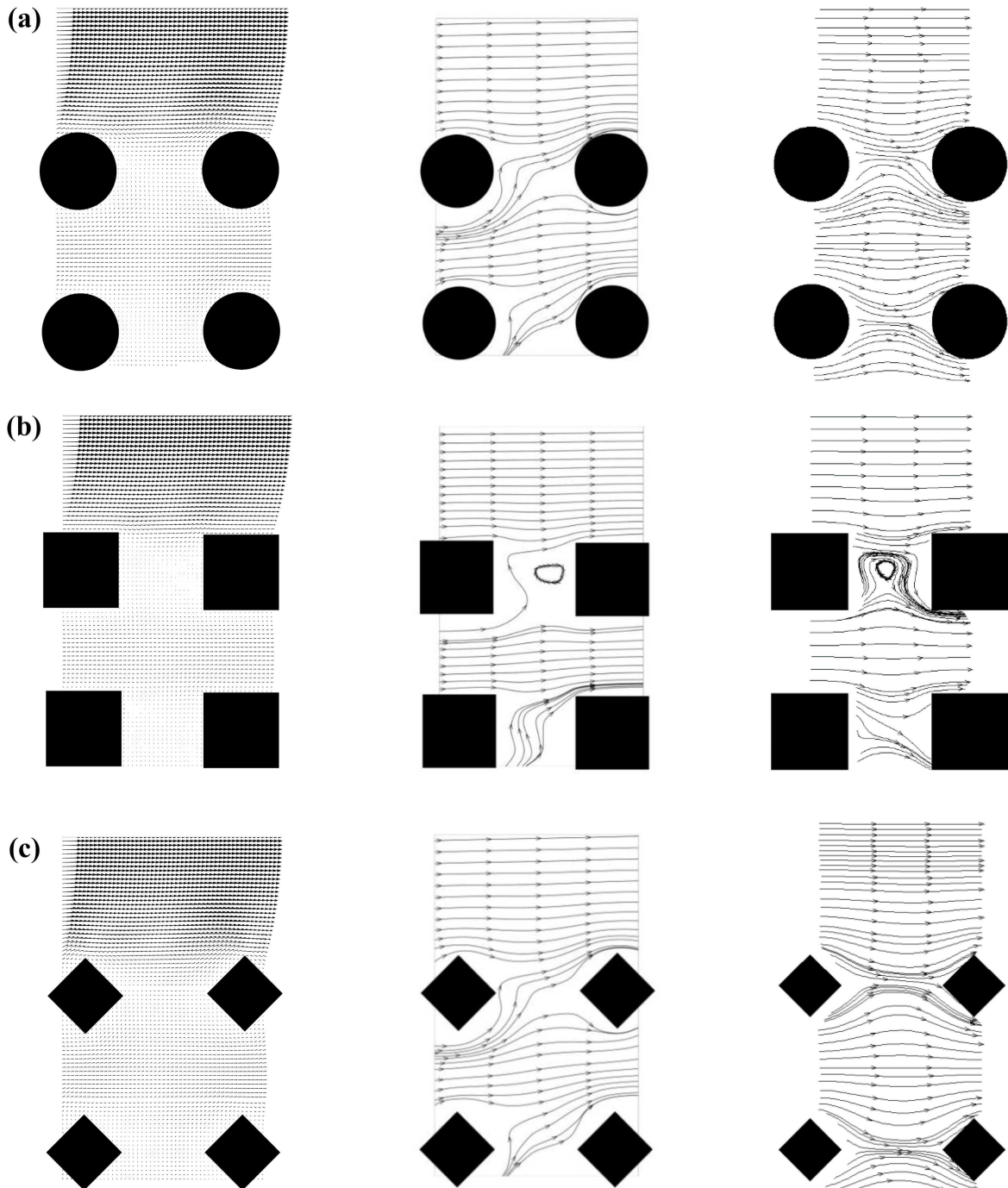


Fig. 7. Typical experimental velocity vector maps, experimental streamlines and numerical streamlines at the interface region from left to right: (a) case-1, (b) case-2, (c) case-3.

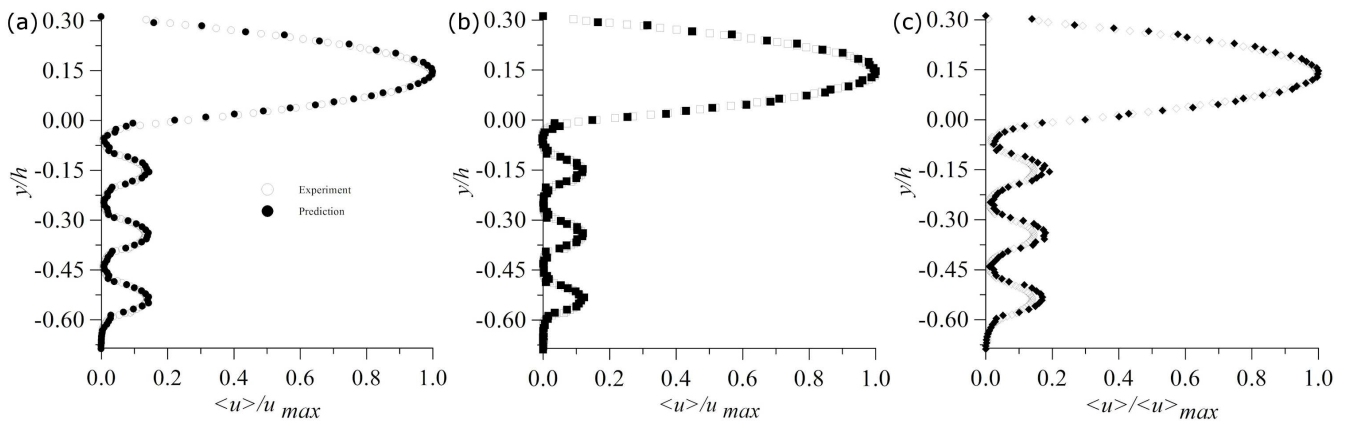


Fig. 8. The vertical averaged profile of horizontal velocity component at  $x = 677$  mm: (a) case-1, (b) case-2, (c) case-3.

The velocity profiles obtained at  $x = 677$  mm of the channel from experimental measurements and numerical computation are compared in Fig. 8. First of all, it is clear from Fig. 8a,b, and c that the numerical and experimental results are best matched for all three cases and the same flow rate. The flow rate is  $0.16 \text{ m}^3/\text{h}$  and is kept constant during the experiments for all three cases. To determine the interface velocity and velocity gradient for the three cases, it is needed to compute the average velocity at various  $y$  locations. The averaging  $y$ -location is obtained in  $x$ -direction for a unit cell as seen in Fig. 2 and using Eq. (11), see [6]:

$$\langle u \rangle = \frac{1}{S} \int_0^S u(y) dx. \quad (11)$$

The averaging ignores the regions blocked by the cylinders. The variation of  $\langle u \rangle$  with  $y$  for circular, square, and  $45^\circ$  rotated square cylinders is illustrated in Fig. 9 near interface region. The velocities decay from the value of interface to an approximately fixed value toward the porous layer. The decay of velocity seems to be more rapid for the case-2 than those for case-1 and case-3. At the same time, the interface velocity for case-2 is less than those for case-1 and case-3. It is evidently understood that the interface velocities are strongly affected by the interface geometry and roughness as mentioned before.

The shear rate  $\gamma = du/dy$  at the interface can be calculated by the least square curve fittings using the area averaged velocity in the interfacial region as seen in Fig. 9. The shear rates, which are calculated by differentiating the best fit curve at  $y = 0$ , are estimated for the three cases as seen in Table I. Other significant experimental and numerical flow parameters are also outlined in Table I. The largest interface velocity and the dimensionless slip velocity belong to case-1 (circular cross-section) while the smallest interface velocity and the dimensionless slip velocity belong to case-2. When solid fraction  $\beta$  in the channel increases,  $u_i/u_{max}$  decreases as expected. This result may be attributed to the sectional shape of rod bundles. While the dimensionless interface velocity reaches the highest value for circular cylinders, it decreases slightly for  $45^\circ$  rotated square cylinders and di-

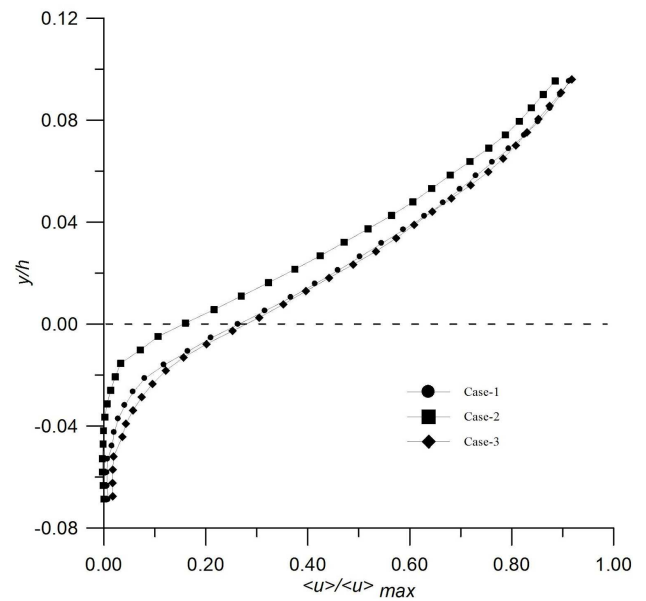


Fig. 9. Area averaged velocity for case-1, case-2, and case-3.

minishes abruptly for square cylinders. Slip coefficient of case-2 (square cylinders) is also markedly greater than the other cases. These results arise from different flow characteristics observed in porous region constructed by square cylinders nearby the interface. Recirculation region between square cylinders of first row nearby the interface region causes a blockage effect on the fluid flow from porous region into the clear fluid region. Based on the complete set of both experimental and computational results, an interpretation of the parameters obtained can be made. If the maximum velocity values of the free fluid zone are compared, square cross-section shows the highest maximum velocity value regarding both experimental and computational results while  $45^\circ$  rotated cross-section yields the lowest value. The same trend is obtained by comparing the velocity gradient. Therefore, it is possible to propose a relationship between maximum velocity and the velocity gradient. The parameters dependent



upon the velocity field and analytically derived permeability are used to obtain the slip coefficient  $\alpha$  which is introduced by Beavers and Joseph [1]. According to both experimental and computational results, circular cross-section shows the lowest  $\alpha$  value while square cross-section shows the highest.

The experimental results of this study are compared with the experimental results obtained by Beavers and Joseph [1] for validation purposes. The present experimental results for three cases accurately predict the experimental data as seen in Fig. 10. The quantity  $\Phi$  was explained in the paper of Beavers and Joseph [1] as the fractional increase in mass flow rate through the channel in Fig. 10. It is defined as:

$$\Phi = \frac{3(\sigma + 2\alpha)}{\sigma(1 + \alpha\sigma)}, \quad (12)$$

where  $\sigma = h_f/\sqrt{k}$  and  $\alpha$  is the slip coefficient.  $\Phi$  can also be computed from the presented experimental results by using Table I. In the experiments of Beavers and Joseph [1], three kinds of foam metal having different permeability were used as seen in Fig. 6 of [1]. In the present experimental study, three different cases as explained before having different permeability are also used as shown in Table I. The analytical and experimental results of Beavers and Joseph [1] agree closely on the present experimental data for our case-1, case-2, and case-3 as shown in Fig. 10. As can be seen from Fig. 10, square cylindrical rods give rise to a remarkable increase in slip coefficient which would diminish fractional increase in mass flow rate  $\Phi$  through the channel. In present experiments filling fraction  $h_p/h$  and  $h_p/S$  values are kept constant. Porosity of tested medium remains between 0.77 and 0.89. Assuming that slight variation in porosity may not show a dominant effect on slip coefficient, this result can be attributed to geometrical structure of porous region. Utilization of rotated square cylindrical shape instead of circular cylinder cause a relatively small increase in slip coefficient.

The variation of dimensionless slip velocity as a function of solid volume fraction is presented in Fig. 11. The present experimental results are compared with the experimental results of [8] and analytical results of [10] for pressure driven flow and different type of cylindrical rod arrangements as seen in Fig. 11. The experimental study of [8] is investigated for brushes which have a height of 7 or 14 mm and the model in the analytical study of [10] is similar to the present experimental investigation. The current results for case-1, case-2, and case-3 are in accordance with the experimental study of [8], having lower dimensionless slip velocities with a higher  $h_p/h$  value. As it is also stated in [8], the analytical study of [10] yields much lower dimensionless slip velocities around 0.23 which is not attainable in experimental investigations. Considering either experimental or analytical studies, Fig. 11 shows also that dimensionless slip velocity does not depend on solid volume fraction as long as the same geometry at a constant  $h_p/h$  is used.

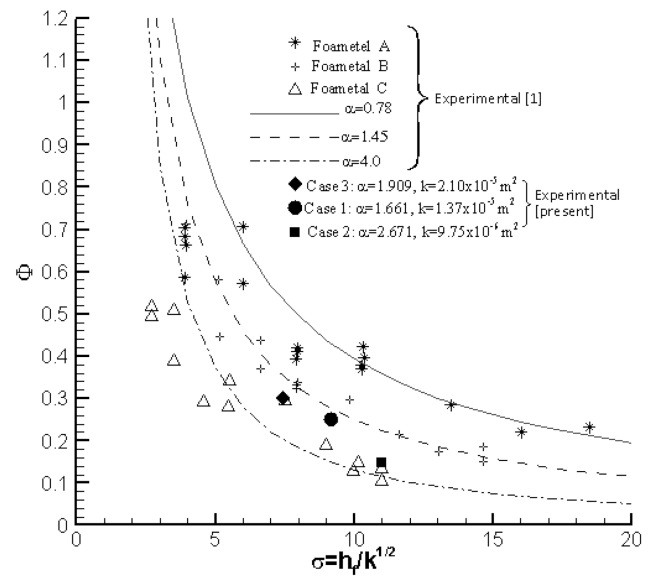


Fig. 10. Comparison between present experimental results and the experimental data of Beavers and Joseph [1].

For the present investigation, although  $h_p/h$  is constant, the three cases have different geometrical structures and yield slightly different dimensionless slip velocities which are expected to remain nearly constant when different solid volume fractions were used. Therefore, an important parameter affecting the dimensionless slip velocity is geometrical structure of porous medium at the interface. As can be seen from Fig. 11, switching circular rod bundles with non-circular ones affects dimensionless slip velocity in a similar manner as increasing filling fraction in channel would.

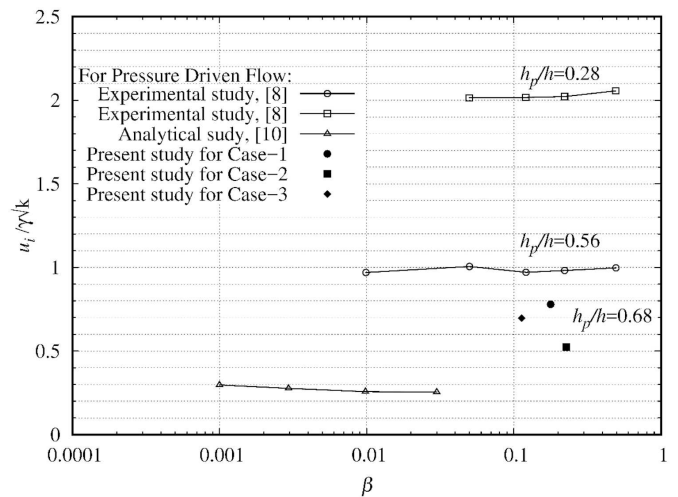


Fig. 11. Variation of  $u_i/\gamma\sqrt{k}$  with solid volume fraction  $\beta$ .

## 6. Conclusion

In this experimental investigation, PIV technique is used to examine the velocity field in a pressure driven flow through a composite channel. The porous layer in the channel consists of acrylic cylindrical rods installed horizontally and perpendicular to the flow direction. To support the experimental results, a numerical study is performed for the same channel geometry using a commercial software. As mentioned before, the velocity field obtained experimentally matches very well with numerical predictions. The Reynolds number is kept smaller than unity during all experiments to satisfy the Darcy flow model. The Reynolds numbers based on the Darcy velocity  $Re_p$  are 0.25, 0.32, and 0.35 for all experiments. Three different cases are investigated to show the effects of the roughness or shape of the interface region on interface (or slip) velocity. During the experiments, a recirculation for square cylinder is observed at the first row or interface region. This kind of recirculation blocks the fluid flow toward the clear region and decreases the slip or interface velocity. It is observed from the experiments that the interface velocity strongly depends on the arrangement on the interface region. The present experimental study shows that the relationship between the slip coefficient  $\alpha$  and the permeability of the porous medium is inversely proportional.

## Acknowledgments

This study has been supported by the Scientific and Technological Research Council of Turkey TUBITAK, with grant 107M592.

## References

- [1] G.S. Beavers, D.J. Joseph, *J. Fluid Mech.* **30**, 197 (1967).
- [2] S.K. Gupte, S.G. Advani, *Exp. Fluids* **22**, 408 (1997).
- [3] B. Alazmi, K. Vafai, *Int. J. Heat Mass Transf.* **44**, 1735 (2001).
- [4] A. Goharzadeh, A. Khalili, B.B. Jorgensen, *Phys. Fluids* **17**, 057102 (2005).
- [5] M. Shams, I.G. Currie, D.F. James, *Exp. Fluids* **35**, 193 (2003).
- [6] M.F. Tachie, D.F. James, I.G. Currie, *J. Fluid Mech.* **493**, 319 (2003).
- [7] M.F. Tachie, D.F. James, I.G. Currie, *Phys. Fluids* **16**, 445 (2004).
- [8] M. Agelinchaab, M.F. Tachie, D.W. Ruth, *Phys. Fluids* **18**, 017105 (2006).
- [9] A. Narasimhan, K.S. Raju, S.R. Chakravarthy, *J. Fluids Eng.* **136**, 04120 (2014).
- [10] D.F. James, A.M.J. Davis, *J. Fluid Mech.* **426**, 47 (2001).
- [11] D.A. Nield, A. Bejan, *Convection in Porous Media*, Springer, New York 2006.
- [12] G.W. Jackson, D.F. James, *Can. J. Chem. Eng.* **64**, 364 (1986).
- [13] A. Tamayol, M. Bahrami, *Int. J. Heat Mass Transf.* **52**, 2407 (2009).
- [14] A.C. Baytas, D. Erdem, H. Acar, O. Cetiner, H. Basci, *J. Porous Media* **15**, 1009 (2012).
- [15] P. Prinos, D. Sofialidis, E. Keramaris, *J. Hydraul. Eng.* **129**, 700 (2003).
- [16] H.C. Chan, W.C. Huang, J.M. Leu, C.J. Lai, *Int. J. Heat Fluid Flow* **28**, 1157 (2007).
- [17] S.V. Patankar, *Numerical Heat Transfer and Fluid Flow*, Hemisphere, New York 1980.